

Elemental mapping in achromatic atomic-resolution energy-filtered transmission electron microscopy



B.D. Forbes^a, L. Houben^b, J. Mayer^{b,c}, R.E. Dunin-Borkowski^b, L.J. Allen^{a,*}

^a School of Physics, University of Melbourne, Parkville, VIC 3010, Australia

^b Ernst Ruska-Centre for Microscopy and Spectroscopy with Electrons and Peter Gruenberg Institute, Forschungszentrum Jülich, D-52425 Jülich, Germany

^c Central Facility for Electron Microscopy, RWTH Aachen University, D-52074 Aachen, Germany

ARTICLE INFO

Article history:

Received 27 March 2014

Received in revised form

27 June 2014

Accepted 6 July 2014

Available online 15 July 2014

Keywords:

Achromatic EFTEM

Elemental mapping

Preservation of elastic contrast

ABSTRACT

We present atomic-resolution energy-filtered transmission electron microscopy (EFTEM) images obtained with the chromatic-aberration-corrected FEI Titan PICO at the Ernst-Ruska Centre, Jülich, Germany. We find qualitative agreement between experiment and simulation for the background-subtracted EFTEM images of the Ti–L_{2,3} and O–K edges for a specimen of SrTiO₃ oriented down the [110] zone axis. The simulations utilize the transition potential formulation for inelastic scattering, which permits a detailed investigation of contributions to the EFTEM image. We find that energy-filtered images of the Ti–L_{2,3} and O–K edges are lattice images and that the background-subtracted core-loss maps may not be directly interpretable as elemental maps. Simulations show that this is a result of preservation of elastic contrast, whereby the qualitative details of the image are determined primarily by elastic, coherent scattering. We show that this effect places a constraint on the range of specimen thicknesses which could theoretically yield directly useful elemental maps. In general, interpretation of EFTEM images is ideally accompanied by detailed simulations.

© 2014 Elsevier B.V. All rights reserved.

1. Introduction

Understanding the structure and composition of materials at atomic resolution is essential in modern science, in a diverse range of fields including materials science, nano-technology and biology. Transmission electron microscopy is well placed to achieve this goal, utilizing electrons with de Broglie wavelengths far smaller than typical interatomic spacings. In addition, instrumentation techniques such as spherical aberration correction are well established [1–3]. High-resolution transmission electron microscopy (HRTEM) is a technique that images a specimen using the elastic scattering of an incident planar wave field. HRTEM routinely allows the determination of structure at atomic-resolution and precision in atomic location even better than this [4]. However, the strong interaction of the incident fast electrons with the electrostatic potential of the specimen often prevents direct interpretation of compositional details from experimental results. Scanning transmission electron microscopy (STEM) imaging modes acquire spatial information sequentially but acquire other information in parallel, including the far-field scattering distribution, electron energy loss spectra (EELS), and secondary x-ray spectra. Specimen composition can be obtained in many cases in STEM using a

high-angle annular dark field (HAADF) detector, which shows Z-contrast [5]. Two-dimensional elemental mapping at atomic resolution has also been demonstrated using STEM EELS, see for example Ref. [6].

Elemental mapping has been performed at less than atomic resolution for wide-field energy-filtered transmission electron microscopy (EFTEM), see for example Refs. [7,8]. In this mode, an energy filter selects for imaging those electrons that have undergone a particular range of energy losses near an ionization edge. In contrast to STEM, here spatial information is acquired in parallel while energy-loss information is acquired sequentially. Chromatic aberrations in the objective lens have in the past prevented EFTEM from achieving atomic resolution, by inducing a defocus spread on the electrons that have lost varying amounts of energy after inelastic scattering. High-resolution EFTEM images could be obtained only by reducing the width of the energy window to counter this effect [9,10], to the detriment of the signal-to-noise ratio and the ability to extract background-corrected elemental maps.

Recently a chromatic aberration corrector has been developed and integrated into the FEI Titan (S)TEM [11–14]. This allows wide energy-filtering windows (with a corresponding increase in signal-to-noise ratio) to be employed with minimal defocus spread and, as such, atomic resolution is now within reach in EFTEM. Atomic-resolution EFTEM imaging has been performed on silicon, resolving the dumbbell structure with 1.35 Å separation [15].

* Corresponding author.

E-mail address: lja@unimelb.edu.au (L.J. Allen).

However, atomic-resolution elemental mapping discriminating between different elements has not yet been demonstrated, since in that work only one element was present. Here we present new results taken with the FEI Titan 60-300 PICO at the Ernst Ruska Centre, studying a specimen of SrTiO₃ oriented down the [110] zone axis. Both the Ti-L_{2,3} and O-K edges were used for imaging. We find qualitative agreement between the experimental results and simulations performed using the transition potential formulation. Simulations show that due to the delocalized nature of the transition potentials associated with these ionization edges, directly interpretable elemental mapping is not possible in this case. Only through detailed simulations can one understand how the features of the image correspond to specimen composition.

2. Experimental results

An energy-filtered transmission electron microscopy spectrum imaging (EFTEM-SI) series for a specimen of SrTiO₃ was acquired using the C_c-corrected FEI Titan PICO at the Ernst Ruska Centre, Jülich, Germany. The specimen was oriented down the [110] zone axis and was estimated to have a thickness of 30 nm using the log-ratio method [16]. The accelerating voltage was 200 kV. The third-order spherical aberration, C_s, associated with the objective lens was tuned to $-6 \mu\text{m}$ in the presence of the fifth-order spherical aberration C_s of 1.5 mm. The C_s coefficient was chosen to provide optimum phase contrast at a small positive defocus of a few nm [17]. No aperture stop was used in the back focal plane of the objective lens. The chromatic aberrations of the objective lens were corrected for 1.0 Å resolution with a uniformly filled 50 eV energy-selecting slit. Series of energy-loss images were recorded with a Gatan GIF Quantum ERC high-resolution imaging filter. An energy window of width 25 eV was shifted in steps of 10 eV for centre-window energies between 390 eV and 560 eV. Each image was acquired in 20 s using a current of 3 nA in a beam with a semi-convergence angle of 2.5 mrad. The Nyquist frequency of the CCD camera was 40 nm⁻¹. The semi-collection angle was larger than 35 mrad, verified by the occurrence of 14 nm⁻¹ Bragg reflections in zero-loss images. The optimal defocus was tuned beforehand using the detail in EFTEM images at an energy loss of about 100 eV. The resulting defocus is coincident with the minimum contrast defocus in a zero-loss-filtered image. This defocus is approximately 2 nm less than the optimal phase contrast defocus of about +4 nm. Fig. 1 shows regions cropped from the EFTEM-SI series of images which have been background-subtracted using a many-window power law method for the Ti-L_{2,3} edge (top) and O-K edge (bottom). (Such background-subtracted images are commonly referred to as maps.) The raw data underwent a series

of processing steps: sub-pixel alignment of the image for each energy window; pixel-wise background fit using a many-window method; background subtraction; and periodic averaging. The image alignment was done using a coarse manual pre-alignment followed by a sub-pixel refinement step that involves the cross-correlation with the principal component of the pre-aligned image series. The background power law was optimized pixel-for-pixel, using a least squares regression to fit the data of six Ti-L_{2,3} pre-edge window positions and three O-K pre-edge images. Optimized and extrapolated background count rates were then calculated for each energy window position and pixel and were subtracted from the raw data to produce the Ti-L_{2,3} and O-K map data. The periodic averaging was applied in order to increase the signal-to-noise ratio due to low electron count rates. It was performed by shifting the source image sub-pixel-wise by a grid of full repeat periods, i.e. a running average with periodic displacement. The average number of electrons above background counted per pixel and per second in a Ti-L_{2,3} core-loss window was approximately 0.6, and in an O-K core-loss window it was approximately 0.2. The average background count rate was about 1.2 electrons per pixel and per second for both core-loss edges.

The EFTEM-SI series which has been background-subtracted for the Ti-L_{2,3} edge (Fig. 1, top row) shows a trend of increasing intensity with the centre-window energy up to 470 eV, whereafter the intensity drops. This trend can be understood as follows. The energy window had a width of 25 eV, and thus had tails of width 12.5 eV extending to either side of the centre-window energy. The edge onset occurs at approximately 458 eV. Therefore, for a 450 eV centre-window energy the upper tail of the window is just barely covering the edge onset; at 460 eV roughly half of the window covers the edge onset; at 470 eV the window is entirely over the edge; and at 480 eV the window covers higher energy losses with a lower cross section. We choose to consider the background-subtracted image for the 470 eV centre-window energy to represent the Ti-L_{2,3} map.

This trend is represented to a lesser extent in the EFTEM-SI series which has been background-subtracted for the O-K edge (Fig. 1, bottom row). This is due to the lower ionization cross-section associated with the O-K edge. For this edge we take the background-subtracted image for a 540 eV centre-window energy to represent the O-K map.

In the experimental images for both edges a lattice is visible. However, neither EFTEM map allows for a direct discrimination of the element of interest; both resemble lattice images. This is due to an effect known as preservation of elastic contrast which has the consequence that EFTEM imaging at atomic resolution may not yield directly interpretable elemental maps [15,18–22]. Direct interpretation of these data as elemental maps may be misleading,

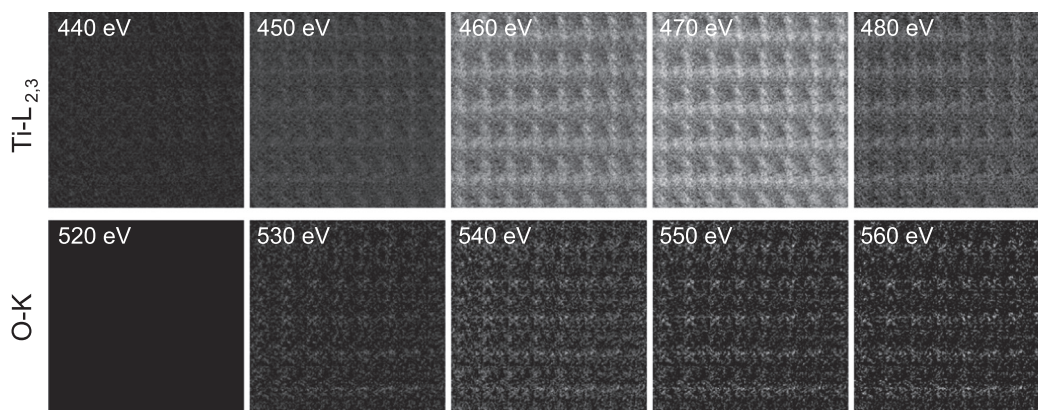


Fig. 1. Energy-filtered transmission electron microscopy (EFTEM) spectrum imaging (SI) series for a specimen of SrTiO₃ oriented down the [110] zone axis. The specimen was estimated to be 30 nm thick. Top: Ti-L_{2,3} edge (edge onset 458 eV). Bottom: O-K edge (edge onset 532 eV). The panels show background-subtracted images.

and simulations are needed to ensure that reasonable conclusions are drawn regarding specimen structure and composition. This is not different from the case in HRTEM wherein the coherent scattering of the incident planar wave field within the specimen leads to a strong dependence of the qualitative features and interpretation of HRTEM images on parameters such as specimen thickness. In the following sections we will use theory and simulation to interpret the EFTEM images and understand what conclusions may be reliably drawn from the data. We also explore whether there are conditions under which direct interpretation *would* be possible.

3. Background theory

In this section we outline the theoretical basis for the simulations to be performed in later sections. Our simulations employ the double-channelling transition potential formulation [22–24]. In this formulation the elastic scattering of the incident fast electron before and after inelastic scattering events is taken into account. In addition, attenuation of the elastic and inelastic waves due to thermal scattering is accounted for using the model due to Hall and Hirsch [25]. The time independent Schrödinger equation for the system comprising the fast electron and specimen is

$$\left[-\frac{\hbar^2}{2m_e} \nabla_{\mathbf{r}}^2 + H_c(\boldsymbol{\tau}) + H'(\mathbf{r}, \boldsymbol{\tau}) \right] \Psi(\mathbf{r}, \boldsymbol{\tau}) = E\Psi(\mathbf{r}, \boldsymbol{\tau}), \quad (1)$$

where \mathbf{r} is the fast electron coordinate, $\boldsymbol{\tau}$ are the coordinates of the nuclei and electrons making up the specimen, $\Psi(\mathbf{r}, \boldsymbol{\tau})$ is the many-body wave function, E is the total energy of the system, $H_c(\boldsymbol{\tau})$ is the crystal Hamiltonian and $H'(\mathbf{r}, \boldsymbol{\tau})$ is the interaction Hamiltonian between the fast electron and the nuclei and electrons in the specimen. The many-body wave function is expanded in the eigenbasis of the crystal Hamiltonian $H_c(\boldsymbol{\tau})$ to yield

$$\Psi(\mathbf{r}, \boldsymbol{\tau}) = \sum_n \psi_n(\mathbf{r}) a_n(\boldsymbol{\tau}), \quad (2)$$

where $\psi_n(\mathbf{r})$ describes the fast electron having left the crystal in a normalized eigenstate $a_n(\boldsymbol{\tau})$ satisfying the equation

$$H_c(\boldsymbol{\tau}) a_n(\boldsymbol{\tau}) = \varepsilon_n a_n(\boldsymbol{\tau}), \quad (3)$$

with the associated crystal energy ε_n . Assuming orthogonality of the crystal eigenbasis, the fast electron probability density at depth z is found to be

$$I(\mathbf{r}_{\perp}, z) = \sum_n |\psi_n(\mathbf{r}_{\perp}, z)|^2, \quad (4)$$

where \mathbf{r}_{\perp} is the transverse coordinate of the fast electron. Eq. (4) is easily modified to account for imaging via the objective lens by convolving each inelastic wave $\psi_n(\mathbf{r}_{\perp}, z)$ with the lens transfer function. The inelastic waves $\psi_n(\mathbf{r}_{\perp}, z)$ are found in the single inelastic scattering approximation to be [23]

$$\psi_n(\mathbf{r}_{\perp}, z) = \frac{m}{2\pi\hbar^2 k_n} H_{n0}(\mathbf{r}_{\perp}) \psi_0(\mathbf{r}_{\perp}, z), \quad (5)$$

where k_n is the wavenumber of the fast electron having lost the energy ε_n in exciting the crystal to state n and $H_{n0}(\mathbf{r}_{\perp})$ is the transition potential between the ground state and excited state n of the crystal, projected in the beam direction. We choose to work in an angular momentum basis to describe the initial (bound) and final (continuum) state wave functions for the electron that is ejected during the ionization process [22]. This choice of basis has the advantage that a relatively small number of transitions are required to achieve a converged calculation, as opposed to, for example, a plane wave basis. The multislice method [26] was used for the calculation of elastic scattering.

4. Simulations

Fig. 2(a) shows the background-subtracted EFTEM image of the Ti-L_{2,3} edge corresponding to a 470 eV centre-window energy (as pictured in Fig. 1). Fig. 3(a) shows the background-subtracted EFTEM image of the O-K edge corresponding to a 540 eV centre-window energy (as pictured in Fig. 1). A Gaussian filter with a standard deviation of two pixels has been applied to remove noise and enable more convenient numerical analysis. Simulations employing the transition potential formulation (as outlined in Section 3) have been overlaid in Figs. 2(a) and 3(a), along with the projected specimen structure. The simulations used the same parameters as the experiment where known: in particular the accelerating voltage was 200 kV, the third-order spherical aberration C_3 was set to $-6 \mu\text{m}$ and the fifth order spherical aberration C_5 was set to 1.5 mm. Plane wave incidence was assumed, although in the experiment the beam semi-convergence angle was roughly 4 mrad and the specimen tilt was around 5 mrad. This beam convergence is not expected to have a significant effect on the elastic and inelastic scattering of the incident electrons. Calculations have been performed which suggest that the specimen tilt does not significantly affect the mechanisms for generating contrast in EFTEM that are detailed in this paper. The objective lens defocus was assumed to be the optimal phase contrast defocus of 4 nm. Calculations for a smaller defocus of 1 nm did not give a significantly better match to the experimental data than the results shown here. The specimen thickness was assumed to be 30 nm, the value suggested by the EELS log-ratio method [16]. A coherent damping envelope was used to impose an information limit of 1.5 \AA^{-1} , due to the intrinsic electrical instabilities in the microscope [27]. A single energy loss of 10 eV above the threshold was assumed for the calculations. In principle, the EFTEM image has contributions from all energy losses lying within the energy window. However, this would result in time-consuming calculations. Previous work has indicated that considering only a single energy loss within the window is reasonably representative of the channelling behaviour of inelastically scattered electrons having lost energies within the whole interval [22,28]. Furthermore, the correction of chromatic aberrations in the experiment negates the need to consider any defocus spread resulting from the large range of energy losses.

Intensity profiles across atomic columns are also shown in Figs. 2(b) and (c) and 3(b) and (c). It is important to note here that the experimental (solid black) lines and simulated (dashed red) lines are not on a common intensity scale, and a quantitative comparison is not intended. However, the experimental lines themselves *are* on a common scale within each figure, as are the simulated lines.

Figs. 2 and 3 demonstrate a favourable qualitative comparison between experimental and simulated EFTEM maps. The simulated Ti-L_{2,3} map correctly predicts higher intensities over the titanium columns than over the oxygen columns, and it also predicts the relatively lower signal found along the strontium-oxygen columns. However, it does seem to overestimate the background signal found between the strontium/oxygen columns as seen in Fig. 2(c). The simulated O-K map overestimates how much intensity remains on the oxygen columns in Fig. 3(b) and between the strontium/oxygen columns Fig. 3(c). These discrepancies can be attributed to a number of factors: low electron count rates and high noise levels in the experimental data; inaccuracies in the assumed values of defocus and specimen thickness; simulations not accounting for the solid state environment of the ionization target or electronic excitations to high-energy unoccupied electron orbitals (also known as the *white lines*); and instabilities and noise in the microscope not accounted for in the calculations.

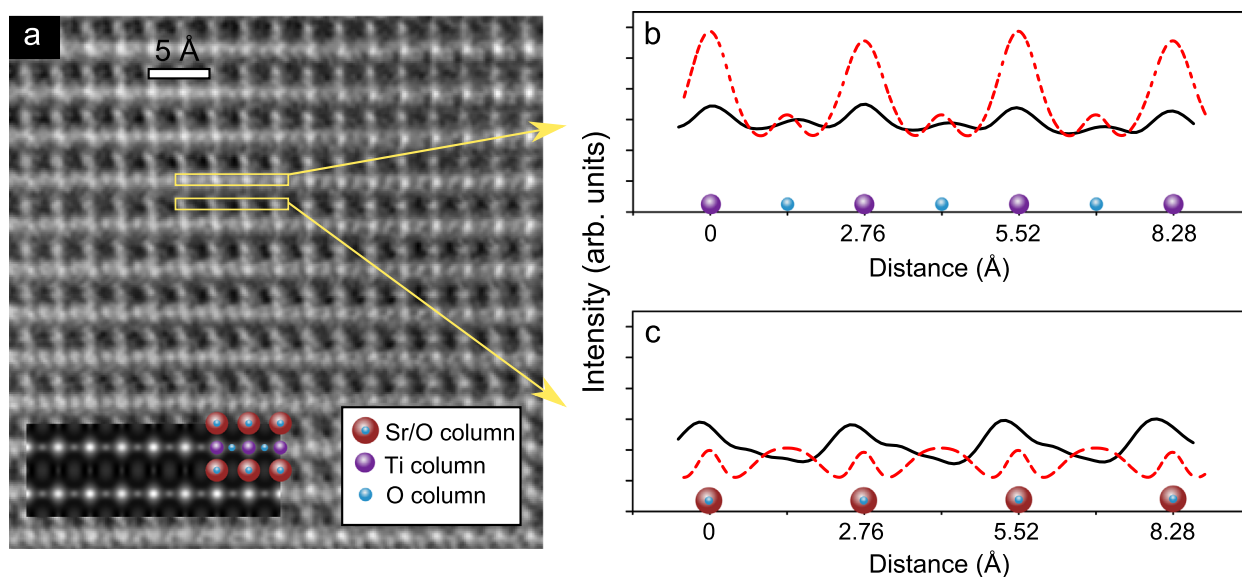


Fig. 2. (a) Background-subtracted EFTEM image of the Ti- $L_{2,3}$ edge for a centre-window energy of 470 eV. A corresponding simulation and specimen structure has been overlaid. Intensity profiles across atomic columns are shown in (b) and (c). These run through Ti-O-Ti and SrO-SrO columns. Solid (black) lines indicate intensity profiles through the experimental map (averaging over a width of 10 pixels) while the dashed (red) lines indicate intensity profiles through the simulated map (averaging over roughly the same spatial width as for the experimental intensity profiles). Both solid (black) lines are on a common scale and both dashed (red) lines are on a common scale. Large (brown) circles indicate strontium atoms, medium (purple) circles indicate titanium atoms and small (blue) circles indicate oxygen atoms. (For interpretation of the references to color in this figure caption, the reader is referred to the web version of this paper.)

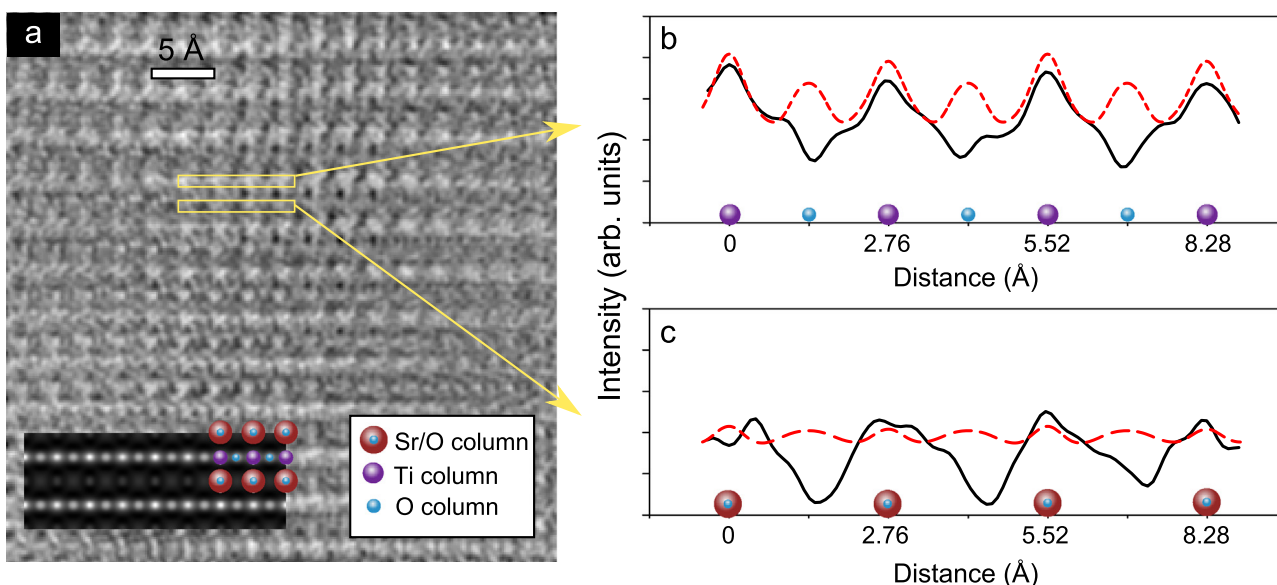


Fig. 3. (a) Background-subtracted EFTEM image of the O-K edge for a centre-window energy of 540 eV. A corresponding simulation and specimen structure have been overlaid. Intensity profiles across atomic columns are shown in (b) and (c). These run through Ti-O-Ti and SrO-SrO columns. Solid (black) lines indicate intensity profiles through the experimental map (averaging over a width of 10 pixels) while the dashed (red) lines indicate intensity profiles through the simulated map (averaging over roughly the same spatial width as for the experimental intensity profiles). Both solid (black) lines are on a common scale and both dashed (red) lines are on a common scale. Large (brown) circles indicate strontium atoms, medium (purple) circles indicate titanium atoms and small (blue) circles indicate oxygen atoms. (For interpretation of the references to color in this figure caption, the reader is referred to the web version of this paper.)

It is clear that the Ti- $L_{2,3}$ map does not give a directly interpretable map of the projected titanium sub-lattice. Significant peaks are found on columns containing only strontium and oxygen. This is due to the delocalization of transition potentials for the Ti- $L_{2,3}$ edge (i.e. ionization at an appreciable distance can occur) which preserves features of the elastic wave function. This is a well-known effect [22] known as preservation of elastic contrast and details specific to our case study will be presented in subsequent sections.

For the O-K map, as in the case of the Ti- $L_{2,3}$ map, qualitative agreement is found, but once again, the EFTEM map does not give

a direct interpretation of the projected oxygen sub-lattice. In fact, there is a large intensity in the vicinity of the titanium columns in the O-K map, while intensity peaks over the oxygen columns are barely distinguishable. The simulations [dashed red line in Fig. 3(b)] reproduce this feature. This is the result of preservation of elastic contrast; elastic scattering (both before and after an inelastic scattering event) causes intensity to be drawn away from the light oxygen columns (where the inelastic waves are generated) and onto the heavy titanium columns. However, for larger thicknesses the reverse trend will occur, with intensity moving away from the titanium columns and back onto the oxygen columns, a

phenomenon known as *Pendellösung*. Thus there may in fact be specimen thicknesses at which the oxygen columns coincide with the most intense features in an O–K map.

5. Discussion

5.1. Localization of elemental information

The experimental data and accompanying simulations presented in Section 4 show that elemental information becomes delocalized in the EFTEM map, in the sense that peaks in intensity do not correspond directly to the location of the elements whose ionization we are considering. Fig. 4 illustrates this delocalization by considering the contribution to the calculated Ti–L_{2,3} map in Fig. 2 due only to ionization events occurring in a single titanium column. An ideal lens is assumed to study the contrast associated with inelastic scattering independent of optical aberrations. The greatest intensity in the map is the central peak around the titanium column in which ionization events occur, but there are additional significant peaks on neighbouring columns up to 3 Å away. These peaks are due to the delocalized transition potentials associated with the Ti–L_{2,3} edge, and the exact mechanism by which the peaks are generated is elucidated below. It is these delocalized features which prevent EFTEM from giving directly interpretable elemental maps. The contribution from any one column of the element of interest is delocalized onto nearby columns as far as 3 Å away. The origin of these peaks lies in the delocalization of transition potentials for the Ti–L_{2,3} edge; a typical case is shown in Fig. 5 for the transition ($l=1, m_l=0$) → ($l'=2, m_{l'}=0$). Fig. 5(a) shows the intensity of the elastic wave function, $|\psi_0|^2$, at a depth of 83 Å as well as the modulus-squared of the transition potential, $|H_{n0}|^2$, while Fig. 5(b) shows the intensity of the resulting inelastic wave, $|\psi_n|^2$. This inelastic wave undergoes further channelling to the exit surface before being imaged, as described in Section 3. The side-peaks noted in Fig. 4 are present when the inelastic wave is first generated; subsequent channelling will further affect how this inelastic wave contributes to the total EFTEM map. This example demonstrates that contrast in the elastic wave function (generated by elastic, coherent scattering) is preserved in the inelastic waves due to the delocalized nature of the transition potentials. One can think of the wave function of the incident electron as simply losing energy in the ionization event and then continuing to propagate with a slightly reduced energy, without the form of the wave having been appreciably changed.

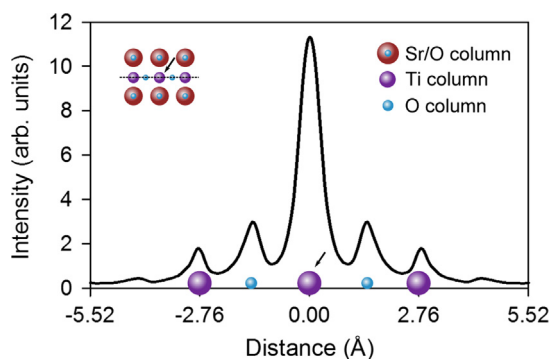


Fig. 4. Intensity profile through a simulated Ti–L_{2,3} EFTEM map considering only Ti–L_{2,3} ionization events occurring within a single titanium column (indicated with an arrow). An ideal lens is assumed for the purpose of investigating the underlying contrast generating mechanisms. The specimen structure is inset (see Fig. 2 for legend) along with the location of the profile (dotted line).

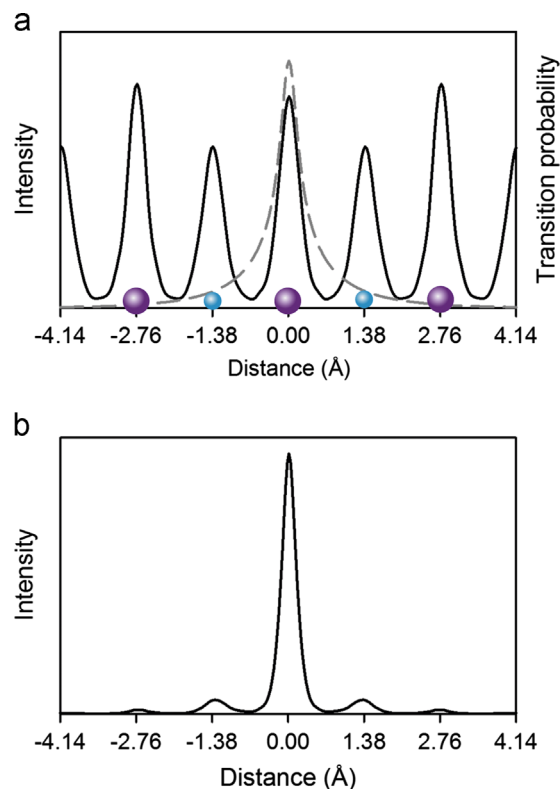


Fig. 5. Generation of an inelastic wave via the ($l=1, m_l=0$) → ($l'=2, m_{l'}=0$) transition at a depth of 15 units cells (83 Å). (a) The solid (black) line shows $|\psi_0(\mathbf{r}_\perp, z)|^2$, the intensity of the elastic wave function, and the dashed (grey) line shows $|H_{n0}(\mathbf{r}_\perp, z)|^2$, the modulus squared of the transition potential. (b) $|\psi_n(\mathbf{r}_\perp, z)|^2$ is the intensity of the inelastic wave generated.

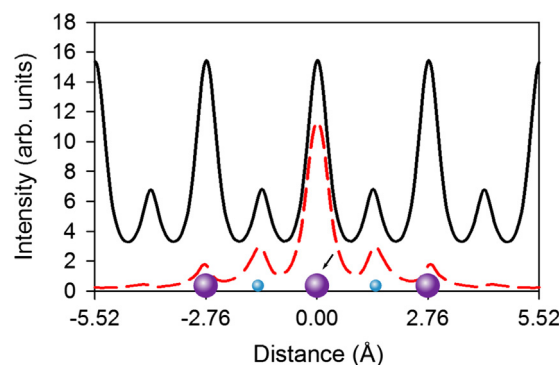


Fig. 6. The result from Fig. 4 tiled along the profile direction, giving a prediction of the actual EFTEM map intensity. The solid (black) line is the tiled result and the dashed (red) line is the single column contribution, repeated from Fig. 4. (For interpretation of the references to color in this figure caption, the reader is referred to the web version of this paper.)

Fig. 4 considers the contributions to the EFTEM map from only one column of atoms. The actual EFTEM map intensity is the incoherent summation of contributions from all columns. This is illustrated in Fig. 6, where we have tiled out the intensity plotted in Fig. 4 to include the intensity contributions from the titanium columns on either side. Careful examination of Fig. 6 shows that the extent to which the EFTEM map contains localized chemical information is reduced significantly by the long-range intensity associated with a single column of the element under investigation. The effect is two-fold: first, a single column on its own has a delocalized contribution; and second, the addition of contributions

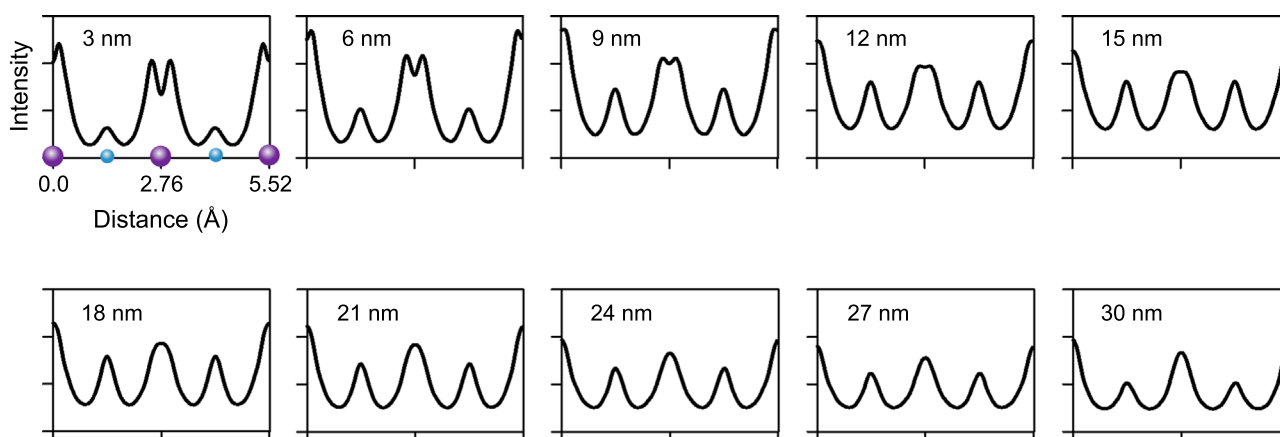


Fig. 7. Simulated intensity profiles in the Ti- $L_{2,3}$ EFTEM map across Ti and O columns for thicknesses up to 30 nm. An ideal lens is assumed. Larger (purple) circles indicate titanium atoms while small (blue) circles indicate oxygen atoms. (For interpretation of the references to color in this figure caption, the reader is referred to the web version of this paper.)

from neighbouring columns increases even further the intensity near columns not containing the element of interest.

5.2. Thickness constraints

The delocalization of the transition potentials associated with the Ti- $L_{2,3}$ edge sets a constraint on the sample thickness required for a localized interpretation of the map. Fig. 7 shows simulated image intensity profiles across titanium and oxygen columns for thicknesses up to 30 nm. It is clear that there is significant delocalization for thicknesses as low as 10 nm. Even for lower thicknesses the maps show intensity peaks on oxygen-only columns. Specimen thicknesses lower than 30 nm are challenging candidates for EFTEM studies due to low electron count rates. Larger specimen thicknesses are better in order to achieve a sufficient count rate and signal-to-noise ratio for a single atomic column given a reasonable accumulation time and electron exposure. As a result, most experimental atomic-resolution EFTEM maps are likely to suffer from some degree of delocalization. Such maps should not be directly interpreted as elemental maps, and should be accompanied by detailed simulations.

5.3. Lens aberrations

Lens aberrations play an important role in the generation of HRTEM and EFTEM images. From the perspective of the transition potential formulation (see Section 3 above), every inelastic wave corresponding to the inelastic events lying within the energy window will be transferred through the imaging plane and will be subject to the same lens aberrations as would an elastically scattered wave field. In particular the intensity measured in the imaging plane can suffer from the usual effects such as delocalization and contrast reversals. In HRTEM, one often thinks of optimizing the contrast transfer function to achieve phase contrast or amplitude contrast conditions [29]. A zero-loss-filtered EFTEM image is a highly coherent image. For a coherent image, an optimized phase plate with a wide passband and a negligible delocalization may be preferred, such as the phase plate for optimal negative phase contrast for weak phase objects [29]. The spatial coherence is in general reduced when higher energy loss processes are involved. In particular, core-loss EFTEM images show a small degree of spatial coherence due to the strong localization of the interaction potential. The image process becomes predominantly incoherent and an optimized amplitude contrast transfer function is the preferred choice. The imaging conditions derived for phase contrast imaging in HRTEM in an aberration-corrected

instrument do in fact result in conditions for EFTEM imaging that are close to optimal. A fairly small spherical aberration coefficient of a magnitude of a few micrometers balanced by a suitable defocus of a few nm is required to achieve optimized phase contrast. A small change in defocus, in our case of 2–3 nm, will produce optimized amplitude contrast for the same spherical aberration coefficient. Hence, the same setting of spherical aberration can be pragmatically used for coherent zero-loss or plasmon-loss filtered images as well as for incoherent core-loss images, with a slight focus correction.

Fig. 8 shows simulated Ti- $L_{2,3}$ images of SrTiO₃ oriented down the [110] zone axis, for thicknesses up to 30 nm, for defoci between -8 and $+8$ nm, and with C_5 at three values, -6 μm , 0 μm , and $+6$ μm . An information limit of 1.5 \AA^{-1} was assumed, which was modelled as a coherent damping envelope applied to the transfer function. Visually, for each value of C_5 there is a defocus where the map is considered optimal, in the sense that it most resembles the specimen structure and is free from artifacts as discussed above. As the coefficient of spherical aberration changes from positive to negative, the optimal defocus changes from negative to positive, in a manner corresponding to the usual optimal conditions used in HRTEM. To demonstrate this, we refer the reader to the three thickness series which are marked by arrows in Fig. 8. These series correspond to the optimal amplitude contrast defocus for each of the three C_5 values used in the calculations. For these EFTEM images there is no significant dependence on C_5 at the corresponding amplitude contrast defocus. The corresponding series at optimal phase contrast defocus are marked by dashed arrows. The small difference in defocus with respect to the optimal amplitude defocus does not change the pattern of the Ti- $L_{2,3}$ image in a noticeable way. The choice of a small value of C_5 is helpful to be able to adjust for optimal phase contrast as well as for optimal amplitude contrast with the need for a slight focus correction only. Therefore the small C_5 for optimized phase contrast is a pragmatic choice that enables the recording of EFTEM data at all energy losses under optimal contrast.

6. Conclusion

New atomic-resolution EFTEM data have been obtained for SrTiO₃ oriented down the [110] zone axis using the C_C -corrected FEI Titan 60–300 PICO at the Ernst Ruska Centre, Jülich, Germany. Background-subtracted EFTEM images of the Ti- $L_{2,3}$ and O-K edges have been obtained and are in qualitative agreement with

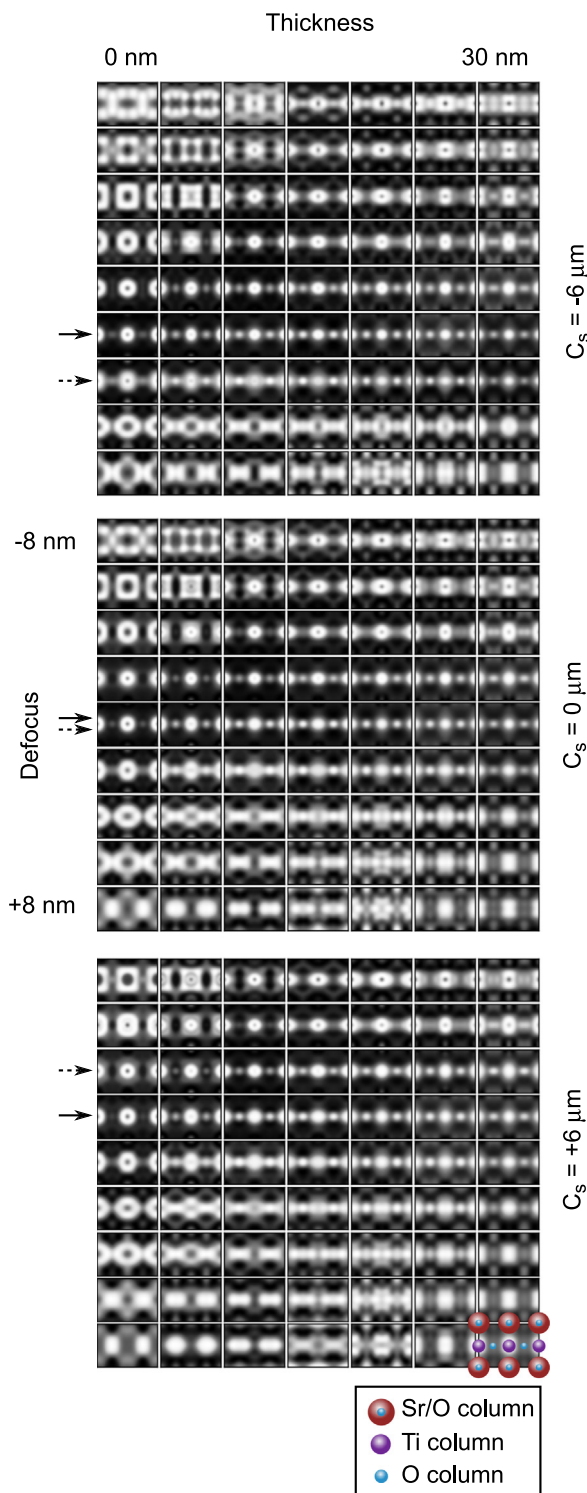


Fig. 8. Simulated Ti-L_{2,3} maps of SrTiO₃ oriented down the [110] zone axis. Each sub-panel is a unit cell, displayed on its own intensity scale. Arrows mark the series at optimal amplitude contrast defocus, and dashed arrows mark the series for optimal phase contrast defocus. The specimen structure has been overlaid at bottom-right.

simulations performed using the transition potential formulation. The maps are not directly interpretable as elemental maps of titanium and oxygen, owing to the effect known as preservation of elastic contrast. Simulations show that due to the delocalized nature of the transition potentials associated with these core-loss edges, a single column of the element of interest makes a

delocalized contribution to the EFTEM image, and in particular intensity is seen around columns as far as 3 Å away from the column in which the inelastic scattering event occurred. Localization of elemental information in the EFTEM maps for the Ti-L_{2,3} and O-K edges is only possible for very thin specimens (≤ 3 nm). However, such thin specimens of SrTiO₃ are challenging candidates for EFTEM studies, since the ionization cross-sections for both edges are small, and the electron count rates may result in an insufficient signal-to-noise ratio. This case study of the Ti-L_{2,3} and O-K edges in SrTiO₃ demonstrates that atomic-resolution EFTEM maps may not give directly interpretable maps of specimen composition and should ideally be accompanied by detailed simulations.

Acknowledgments

This research was supported under the Discovery Projects funding scheme of the Australian Research Council (Project no. DP110102228).

References

- [1] H. Rose, Outline of a spherically corrected semiaplanatic medium-voltage transmission electron-microscope, *Optik* 85 (1990) 19–24.
- [2] M. Haider, S. Uhlemann, E. Schwan, H. Rose, B. Kabius, K.W. Urban, Electron microscopy image enhanced, *Nature* 392 (1998) 768–769.
- [3] O. Krivanek, N. Dellby, A. Lupini, Towards sub-Å electron beams, *Ultramicroscopy* 78 (1999) 1–11.
- [4] L. Houben, A. Thust, K.W. Urban, Atomic-precision determination of the reconstruction of a 90° tilt boundary in YBa₂Cu₃O_{7- δ} by aberration corrected HRTEM, *Ultramicroscopy* 106 (2006) 200–214.
- [5] S.J. Pennycook, L.A. Boatner, Chemically sensitive structure-imaging with a scanning transmission electron microscope, *Nature* 336 (1988) 565–567.
- [6] M. Bosman, V.J. Keast, J.L. Garcia-Munoz, A.J. D'Alfonso, S.D. Findlay, L.J. Allen, Two-dimensional mapping of chemical information at atomic resolution, *Phys. Rev. Lett.* 99 (2007) 086102.
- [7] W. Jäger, J. Mayer, Energy-filtered transmission electron microscopy of Si_mGe_n superlattices and SiGe heterostructures I. Experimental results, *Ultramicroscopy* 59 (1995) 33–45.
- [8] F. Hofer, W. Grogger, P. Warbichler, I. Papst, Quantitative energy-filtering transmission electron microscopy (EFTEM), *Microchim. Acta* 132 (2000) 273–288.
- [9] B. Freitag, W. Mader, Element specific imaging with high lateral resolution: an experimental study on layer structures, *J. Microsc.* 194 (1999) 42–57.
- [10] J. Verbeeck, P. Schattschneider, A. Rosenauer, Image simulation of high resolution energy filtered TEM images, *Ultramicroscopy* 109 (2009) 350–360.
- [11] B. Freitag, S. Kujawa, P. Mul, J. Ringnald, P. Tiemeijer, Breaking the spherical and chromatic aberration barrier in transmission electron microscopy, *Ultramicroscopy* 102 (2005) 209–214.
- [12] H. Rose, Future trends in aberration-corrected electron microscopy, *Philos. Trans. R. Soc. A: Math. Phys. Eng. Sci.* 367 (2009) 3809–3823.
- [13] B. Kabius, P. Hartel, M. Haider, H. Müller, S. Uhlemann, U. Leobauer, J. Zach, H. Rose, First application of C_c-corrected imaging for high-resolution and energy-filtered TEM, *J. Electron Microsc.* 58 (2009) 147–155.
- [14] M. Haider, P. Hartel, H. Müller, S. Uhlemann, J. Zach, Information transfer in a TEM corrected for spherical and chromatic aberration, *Microsc. Microanal.* 16 (2010) 393–408.
- [15] K.W. Urban, J. Mayer, J.R. Jinschek, M.J. Neish, N.R. Lugg, L.J. Allen, Achromatic elemental mapping beyond the nanoscale in the transmission electron microscope, *Phys. Rev. Lett.* 110 (2013) 185507.
- [16] T. Malis, S.C. Cheng, R.F. Egerton, EELS log-ratio technique for specimen-thickness measurement in the TEM, *J. Electron Microsc. Tech.* 8 (1988) 193–200.
- [17] M. Lentzen, Contrast transfer and resolution limits for sub-Ångstrom high-resolution transmission electron microscopy, *Microsc. Microanal.* 14 (2008) 16–26.
- [18] A.J. Craven, C. Colliex, The effect of energy-loss on phase contrast, in: *Institute of Physics Conference Series*, vol. 36, IOP Publishing, Bristol, 1977, pp. 271–274.
- [19] H. Endoh, H. Hashimoto, Y. Makita, Theoretical and observed electron microscope images of impurity atoms in thin crystals formed by L-shell ionization electrons, *Ultramicroscopy* 56 (1994) 108–120.
- [20] T. Navidi-Kasmai, H. Kohl, Computation of contrasts in atomic resolution electron spectroscopic images of planar defects in crystalline specimens, *Ultramicroscopy* 81 (2000) 223–233.
- [21] K. Kimoto, Y. Matsui, Experimental investigation of phase contrast formed by inelastically scattered electrons, *Ultramicroscopy* 96 (2003) 335–342.

- [22] N.R. Lugg, B. Freitag, S.D. Findlay, L.J. Allen, Energy-filtered transmission electron microscopy based on inner-shell ionization, *Ultramicroscopy* 110 (2010) 981–990.
- [23] W. Coene, D. van Dyck, Inelastic scattering of high-energy electrons in real space, *Ultramicroscopy* 33 (1990) 261–267.
- [24] C. Dwyer, Multislice theory of fast electron scattering incorporating atomic inner-shell ionization, *Ultramicroscopy* 104 (2005) 141–151.
- [25] C.R. Hall, P.B. Hirsch, Effect of thermal diffuse scattering on propagation of high energy electrons through crystals, *Proc. R. Soc. Lond. Sect. A* 286 (1965) 158.
- [26] J.M. Cowley, A.F. Moodie, The scattering of electrons by atoms and crystals. I. A new theoretical approach, *Acta Crystallograph.* 10 (1957) 609–619.
- [27] J. Barthel, A. Thust, Quantification of the information limit of transmission electron microscopes, *Phys. Rev. Lett.* 101 (2008) 200801.
- [28] S.D. Findlay, P. Schattschneider, L.J. Allen, Imaging using inelastically scattered electrons in CTEM and STEM geometry, *Ultramicroscopy* 108 (2007) 58–67.
- [29] K.W. Urban, C.-L. Jia, L. Houben, M. Lentzen, S.-B. Mi, K. Tillmann, Negative spherical aberration ultrahigh-resolution imaging in corrected transmission electron microscopy, *Philos. Trans. R. Soc. A: Math. Phys. Eng. Sci.* 367 (2009) 3735–3753.